



Low-thickness Ti–Mn–Zn-substituted Ba-hexaferrite/MWCNT nanocomposites with enhanced magnetic, dielectric, and microwave absorption properties

Seyed Mahmood Tabatabaei Fard^a, Mahmood Moradi^b , Mohammad Mehdi Golshan^c

Department of Physics, College of Science, Shiraz University, Shiraz 71946-84795, Iran

Received: 21 June 2022 / Accepted: 17 October 2022

© The Author(s), under exclusive licence to Società Italiana di Fisica and Springer-Verlag GmbH Germany, part of Springer Nature 2022

Abstract In this work, the various concentrations of Ti, Mn, and Zn were substituted instead of ferric cation of M-type Ba-hexaferrite through the modified sol–gel auto-combustion synthesis procedure. The resulting nanoparticles were compounded with multi-walled carbon nanotubes (MWCNTs), and thus, the BaTi_{2x}Mn_xZn_xFe_{12–4x}O₁₉/MWCNT ($x = 0.0, 0.2, 0.3, 0.4,$ and 0.5) nanocomposites were formed. With the help of Rietveld refinement on XRD patterns in FullProf software, the successful substitution of cations in the single-phase hexagonal lattice structure was confirmed, and the tendency of each cation to occupy five ferric ion sites was investigated. The FTIR analysis was employed to recognition of chemical bonds and confirmation of crystalline structure. FE-SEM and TEM images confirmed the presence of nanoparticles sticking to MWCNTs and homogenous dispersing. The VSM analysis showed that the overall trends of M_S , M_r , and H_C are descending with increasing x , except for a few points described according to the refinement results. The nanocomposites exhibited appropriate microwave absorption properties at the whole X and Ku frequency bands by thickness change of only 0.8 mm. The minimum reflection loss was achieved to -31.5 dB (equivalent to more than 99.9% energy absorption) at a low thickness of just 0.9 mm, and the maximum bandwidth reached 3.89 GHz. As a result, these developed nanocomposites are recommended for use in equipment such as aircraft and UAVs, where the thickness and weight of the absorbing material are of particular importance.

1 Introduction

Due to the evolution of radars and the worldwide employment of electronic equipment, the development of microwave-absorbing materials has become inevitable. This development is used for a variety of purposes, such as EMI (electromagnetic immunity) shielding, radar invisibility (stealth), human and environmental health, and electronic information security considerations [1–6]. Microwave-absorbing layers are placed on the outside body of military vehicles and aircraft to reduce the probability of detection by enemy radars by decreasing the radar cross section (RCS). Superior absorbents with strong absorption, low thickness, low density, and wide bandwidth are in high demand for microwave absorption (MA) applications to eliminate unwanted electromagnetic (EM) waves [7–10]. The synthesis of high-performance MA materials is achieved by adjusting and controlling the composition and microstructure. In fact, by doing this, their electromagnetic parameters, such as magnetic permeability, electrical permittivity, and so on, are optimized [11, 12].

One of the material categories used for MA applications is ferrites. These materials have significant magnetic losses, poor electrical conductivity, relatively low density, and low manufacturing costs. One type of ferrites is hexagonal ferrites, called hexaferrite, discovered in 1952 and is categorized into six groups of crystal structures named X, Y, Z, U, W, and M. Between them, M-type Ba-hexaferrite, BaFe₁₂O₁₉, commonly known as BaM, is a permanent magnet with a magnetoplumbite crystal structure and P6₃/mmc space group [13]. It has adequate potential for MA applications due to some distinct specifications such as outstanding chemical stability, high saturation magnetization, large Curie temperature, uniaxial magnetocrystalline anisotropy, and appropriate hysteresis loop. However, there is significant inequality between the permeability and permittivity of BaM, which leads to the impedance mismatching and non-ideal absorption performance of the pure type of it [6, 14, 15]. Efforts are made to maximize impedance matching and improve MA performance by promoting magnetic and dielectric losses caused by various methods such as adding impurities to BaM or compounding with some dielectric materials such as carbon nanotubes (CNTs) [10, 16–18]. Studies show that substituting multivalent cations instead of Fe⁺³ and Ba⁺² in the BaM compound improves the magnetic and dielectric properties [19–21]. In addition, the substitutions shift the magnetic resonance frequency from the higher values (47.6 GHz for the pure BaM

^a e-mail: mahmood.t383@gmail.com

^b e-mail: mmoradi@shirazu.ac.ir (corresponding author)

^c e-mail: golshan@susc.ac.ir

[22]) to the lower desired frequency bands and also reduce the minimum reflection loss (RL_{\min}) to larger negative values. For example, in one of the recent works where Fe^{+3} has been substituted with different concentrations of Co^{+2} , Ti^{+4} , and Mn^{+2} cations in the BaM structure, the value of RL_{\min} is achieved to -40.2 dB at the thickness of 2.3 mm, and the maximum bandwidth ($RL < -10$ dB) is reached to 7.0 GHz [23].

The addition of multi-walled carbon nanotubes (MWCNTs), which are the low-density carbon-based dielectric, to BaM, increases the dielectric losses and hence increases the absorption of BaM-MWCNT composite. Moreover, multiple reflections of the electromagnetic waves from different walls improve MA performance [24].

Combining hexaferrite with a different volume percentage of MWCNT enables controlling the dielectric constant of the composite and thus impedance more effectively. Therefore, due to the dependency of the RL formula on impedance and thickness of the absorbent, it makes it possible to observe the minimum RL at the lower thicknesses. For example, in another research paper, RL_{\min} reached -47.4 dB with a bandwidth of 4.59 GHz only at a thickness of 1.5 mm [25].

A special focus must be placed on ferrites' microstructure and synthesis methods. There are various methods to synthesis ferrites such as solid-state reaction [26], co-precipitation [19], hydrothermal [27], microemulsion [28], sol-gel [29]. Meanwhile, nanoferrites are agglomerated due to dipolar interactions between particles. Therefore using a method that allows the maximum separation of particles, as well as the formation of small particle size and appropriate morphology, can contribute to improving absorption properties [30]. In some works, done by the solid-state reaction method, Fe^{+3} was substituted with some different dual-dopant cations. The dual-dopant $Zn^{+2}-Ti^{+4}$ and $Mn^{+2}-Ti^{+4}$ had smaller particle sizes and better RL_{\min} comparing to others [31, 32].

In this study, a new nanocomposite containing Ba-hexaferrite substituted with different concentrations of divalent and tetravalent cations Ti^{+4} , Mn^{+2} , and Zn^{+2} , with functionalized multi-walled carbon nanotubes, $BaTi_{2-x}Mn_xZn_xFe_{12-4x}/MWCNT$, was synthesized via the sol-gel technique. The structural, morphological, magnetic, dielectric, and MA qualifications have been investigated, and the correlation of these properties has been evaluated. The initial reason for choosing the Ti^{+4} and Mn^{+2} impurity ions is the reduction of magnetic interactions, thereby magnetization, magnetic anisotropy, and particle size of substituted BaM [23, 33]. These factors shift down the resonance frequency to demanded frequency bands for the MA applications and improve (reduce) the RL_{\min} . The Zn^{+2} impurity cation has a relative tendency to occupy bipyramidal 2b and the octahedral 4f2 sites in the BaM crystal structure, and Fe^{+3} also has upward and downward spins in these two sites, respectively [34]. Therefore, the competition of Zn^{+2} as a non-magnetic cation with other ones for substitution instead of Fe^{+3} determines the increase or decrease of magnetization and anisotropy field according to the substituted site.

Simultaneously usage of these three dopants is a new work and has not been observed in our literature reviews. Moreover, the combination of this new nanoferrite with MWCNT is intended to improve MA parameters, especially at low thicknesses, and it enhances the innovation of this research by itself.

2 Experimental procedure

2.1 Preparation of nanoparticles

Substituted BaM nanoparticles with a chemical formula of $BaTi_{2-x}Mn_xZn_xFe_{12-4x}O_{19}$ ($x = 0.0, 0.2, 0.3, 0.4,$ and 0.5) were manufactured according to the modified sol-gel auto-combustion technique. For every value of x , raw materials were weighed and poured into 300 ml of deionized water at about 70 °C with stoichiometric considerations. The raw materials were $Ba(NO_3)_2$, $Fe(NO_3)_3 \cdot 9H_2O$, $MnCl_2 \cdot 4H_2O$, $Zn(NO_3)_2 \cdot 4H_2O$, and $TiCl_4$. While adding each precursor to the solution, the stirrer was working to homogenize the solution. Precursors were added sequentially to ensure that there was no disruption in the dissolution process. The anhydrous citric acid ($C_6H_8O_7$) was poured into the solution according to the moles of metal cations present. After a few more minutes of stirring, ammonium hydroxide (NH_4OH) 25% was dropped slowly until the pH decreased to 7. The time rate of adding NH_4OH and the final pH value are effective on the final particle size. The temperature was raised to 80 °C for the solution, and after about 1.5 h, it slowly formed a gummy gel. The heater temperature was raised to 100 °C, and after a few minutes, the combustion occurred, and a porous filiform powder was attained. The resulting powder was ground in a porcelain mortar and finally sintered at 900 °C in a furnace so that the heating rate was 4 °C/min and staying at the final temperature was 2 h. What resulted were the M-type hexaferrite nanoparticles. It is essential to adjust the proper sintering temperature profile and the adequate staying temperature to fully form the hexaferrite crystallographic phase and achieve the smallest possible crystallites and particle sizes at the same time.

2.2 Preparation of nanocomposites

The $-COOH$ -functionalized MWCNT was used to transform the hexaferrite nanoparticles into nanocomposites. For this purpose, firstly, a weighed amount of MWCNT at a ratio of 15% by volume of ferrites was sprinkled into the 150 ml deionized water and sonicated at 230 watts for 30 min. Hexaferrite nanoparticles were then added to the suspension, and all were sonicated for 30 min and rested for 10 min. This process was repeated three times to ensure the dispersion of contents and binding of nanoparticles to the MWCNTs. Finally, the suspension was placed within the oven at about 100 °C for water loss, and consequently, the nanocomposite of ferrites and nanotubes was obtained. Ultrasonic power, applying time, and the number of repetitions of the process, are the significant

Table 1 The lattice constants, a and c , cell volume (V_{cell}), lattice constants ratio (c/a), and crystallite size (D) for several concentrations of impurities (x)

x	a (Å)	c (Å)	c/a	V_{Cell} (Å ³)	D (nm)
0.0	5.892	23.214	3.940	697.9	41.75
0.2	5.895	23.205	3.936	698.4	41.73
0.3	5.895	23.214	3.938	698.7	41.74
0.4	5.896	23.218	3.938	699.1	41.74
0.5	5.898	23.223	3.937	699.6	41.74

parameters that ensure the formation of a homogenous nanocomposite. Also, in order to achieve the appropriate microwave absorption specification, which will be described later, it is vital and decisive to use the right amount of carbon nanotubes.

2.3 Preparation of ring-shaped piece for MA analysis

A ring-shaped piece had to be made for the measurement of the microwave scattering parameters (S_{ij}) and thus the complex permeability (μ_r^*), permittivity (ϵ_r^*), and reflection loss (RL) at X and Ku bands by the vector network analyzer. For this purpose, the nanocomposites and melted paraffin were homogeneously mixed with the weight ratio of 80:20 with the assistance of toluene as the diluent. Then the suspension was put into the oven at 70 °C to accelerate the evaporation of toluene. Finally, the shaping mold was filled by resulted mixture and pressed to yield ring shape piece with a thickness of 2 mm, an inner diameter of 3 mm, and an outer diameter of 7 mm.

3 Results and discussion

3.1 Structural, morphological, and chemical bonds properties

The structural and crystallographic properties of nanocomposites have been investigated by XRD analysis with Cu-K α radiation ($\lambda = 1.540$ Å). The X-ray intensity versus 2θ was measured, and then Rietveld refinement was performed on data step by step using FullProf software to achieve the most compatible fitting curve. One of the results of this analysis is to estimate the preference site of impurities instead of Fe⁺³ in the hexaferrite crystal structure, and another is obtaining the hexagonal lattice parameters. In Table 1, structural parameters attained primarily through Rietveld refinement, except for the crystallite size, which is determined by X'Pert software. There are five crystallographic locations for Fe⁺³, ferric ions, in the BaM crystal structure called 2a, 2b, 4f1, 4f2, and 12 k, respectively. The tendency of substituted ions to occupy these sites is not the same. To determine the tendency of impurities for substitution at Fe⁺³ sites, five alternative crystallographic sites were defined for each Ti⁺⁴, Mn⁺², and Zn⁺² ion in FullProf software, and the occupancy of each site was investigated at the end of the refinement process.

Figure 1 displays the XRD patterns of nanoparticles, which all are in a single hexaferrite phase with almost no extra crystallographic phases. Rietveld refinement on XRD patterns showed that Ti⁺⁴ has preferred to replace Fe⁺³ at site 5 (12 k) more than other sites, and Zn⁺² has tended to occupy site 1 (2a). The tendency of Mn⁺² to occupy the sites is almost equivalent, and it has no preference for occupying any particular site.

The ionic radius of Fe⁺³, Ti⁺⁴, and Zn⁺² is 69, 74.5, and 88 pm, respectively, on 1 (2a) and 5 (12 k) sites where the crystal structure is octahedral. As shown in Table 1 and Fig. 2, since the radius of the substituted ions is greater than Fe⁺³, the overall trend of the hexagonal lattice constant c in the substituted specimens is ascending with increasing x . However, the hexagonal lattice constant a is almost unchanged. As an exception to the above trend, it is seen that the sample $x = 0.2$ has a smaller c value than the pure one ($x = 0$). This exception seems to be due to the higher occupancy factor of Ti⁺⁴ in site 4 (4f2) for sample $x = 0.2$ compared to other samples, which is one of the results of the refining process. The 4f2 site is tetrahedral, and the ionic radii of Fe⁺³ and Ti⁺⁴ at this site are 63 and 56 pm, respectively, so the replacement of iron with titanium at this site has resulted in a reduction of the c value [35].

Figure 3 displays the FE-SEM images of BaTi_{2x}Mn_xZn_xFe_{12-4x}/MWCNT ($x = 0.0-0.5$) nanocomposites. The nanoparticles usually have irregular shapes as seen in the picture. However, the presence of some more grown hexagonal shapes confirms the formation of crystallized BaM. The nanoparticles are optimally dispersed between the nanotubes. Some agglomeration has occurred due to magnetic interactions and thus crystal growth; however, the average particle size of nanoparticles is about one hundred nanometers. Electrostatic interaction between cations in the BaM structure and negative charges of the COOH functional group on the outside of MWCNTs has led to the sticking of some nanoparticles across the length of MWCNTs. To better observe this bonding, transmission electron microscopy (TEM) was applied (Fig. 4). In these pictures sticking of nanoparticles, less than 30 nm, to the outer surface of MWCNTs can be seen clearly.

Fourier transform infrared spectroscopy (FTIR) was employed to validate the formation of BaM crystal structure and to identify the chemical bonds. Figure 5 shows the FTIR spectra in the wavenumber range of 400–4000 Cm⁻¹ for pure BaM nanoparticles and BaTi_{2x}Mn_xZn_xFe_{12-4x}/MWCNT nanocomposite for the various concentrations of dopants. There are two absorption peaks at

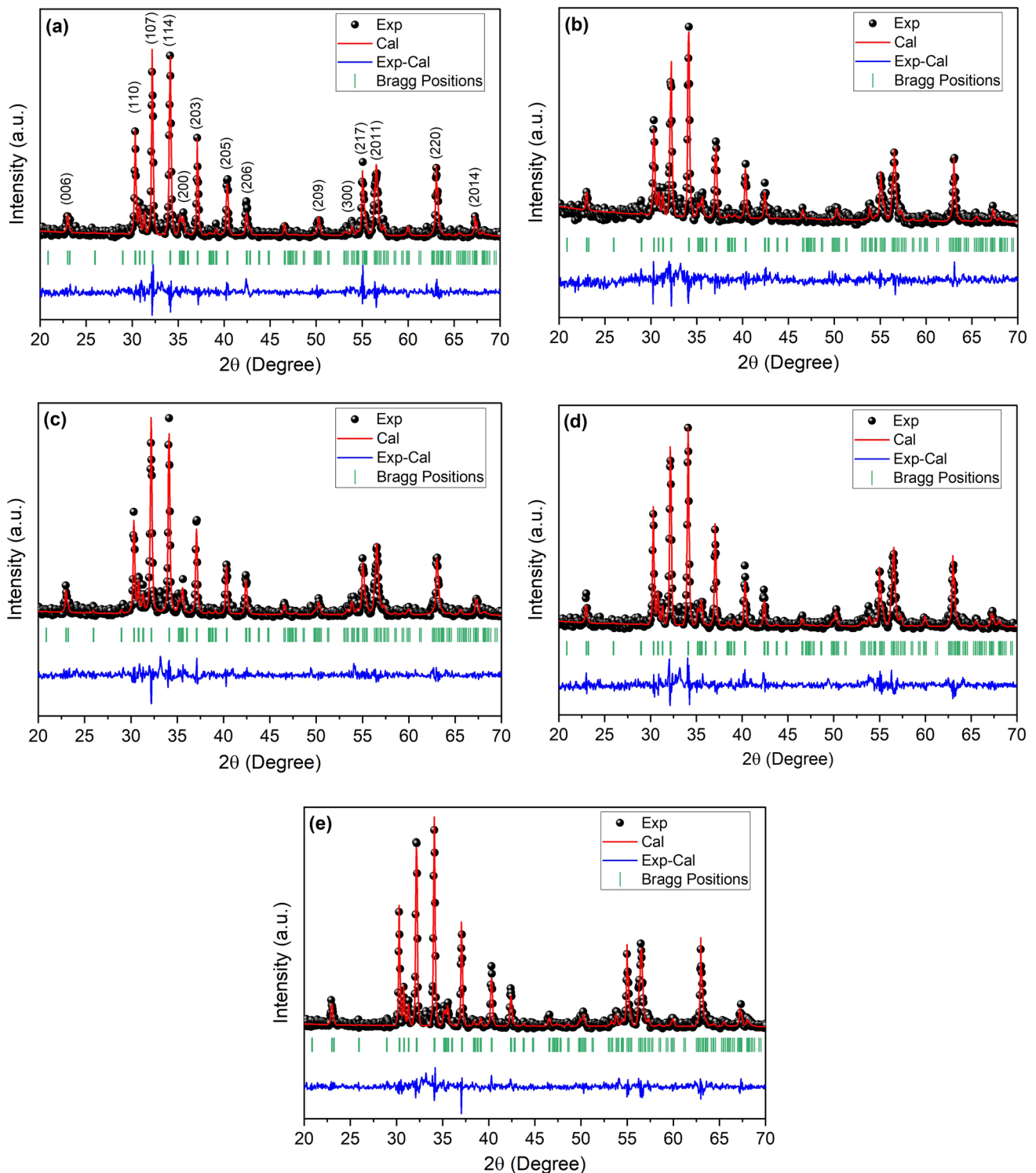
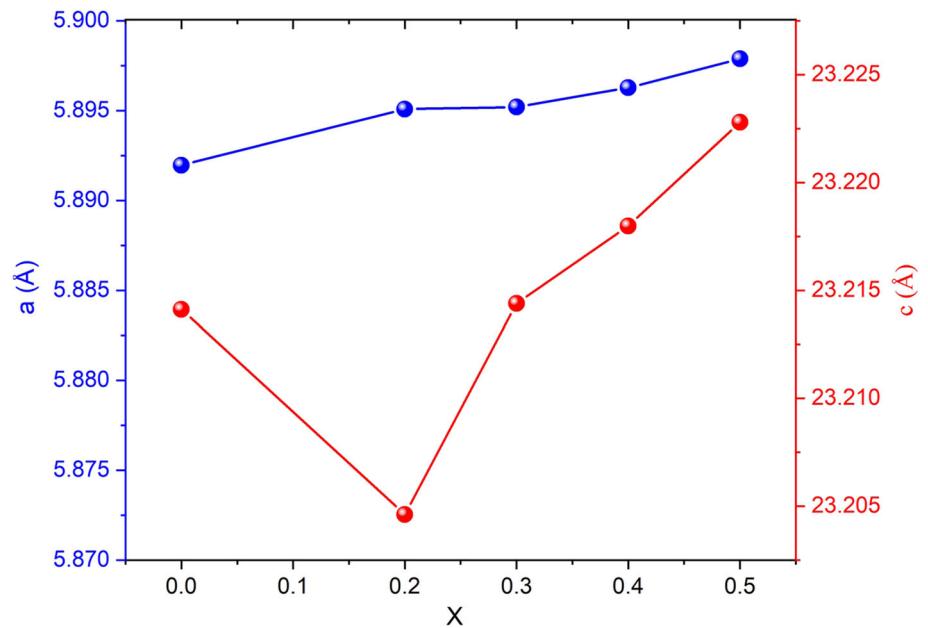


Fig. 1 A Rietveld refinement on XRD patterns of $\text{BaTi}_{2x}\text{Mn}_x\text{Zn}_x\text{Fe}_{12-4x}\text{O}_{19}$ nanoparticles at **a** $x = 0.0$, **b** $x = 0.2$, **c** $x = 0.3$, **d** $x = 0.4$, and **e** $x = 0.5$

about the wavenumber of 434.70 cm^{-1} and 591.45 cm^{-1} , related to oxygen-metal stretching vibration like Fe–O in tetrahedral and octahedral locations, respectively [36, 37]. The peak at about the wavenumber 550.01 cm^{-1} relates to the Ba–O stretching vibration. As shown in this figure, with increasing impurities, the redshift of the Fe–O peak (591.45 cm^{-1}) occurred, and the absorption peak of 550.01 cm^{-1} is gradually eliminated. The redshift of the Fe–O peak on doped-composite samples is due to the replacement of some ferric cations by dopant ions, and it is also due to the intermolecular forces across the substituted ions and other ingredients of the composite [38]. Other peaks in the interval of $850\text{--}1400\text{ cm}^{-1}$ are related to the vibrations of metal–oxygen–metal bonds (M–O–M)

Fig. 2 Hexagonal lattice parameters, a and c , for different concentrations of impurities (x)



such as Fe–O–Fe [36, 37]. The small absorption peaks, seen only in the hexaferrite-MWCNT composites at 1615.55 cm^{-1} and 1797.5 cm^{-1} , are associated with the stretching vibration of C=C and C=O bonds in the cyclic carbonate groups, respectively [38, 39]. These two peaks are not seen in the pure non-composite sample.

The absorption peaks at about 2921.77 cm^{-1} , 3408.14 cm^{-1} , and 3510.79 cm^{-1} correspond to the stretching vibration modes of C–H, stretching vibration of surface OH groups, and other stretching vibration of –OH, respectively [25, 40, 41].

3.2 Magnetic specifications

It was applied the VSM analysis to measure the magnetic specifications. Figure 6a exhibits the M-H hysteresis curve at room temperature for the $\text{BaTi}_{2x}\text{Mn}_x\text{Zn}_x\text{Fe}_{12-4x}/\text{MWCNT}$ samples with various amounts of impurities. Figure 6b represents the graph of saturation magnetization (M_S), remanent magnetization (M_r), and coercivity (H_C) versus doping amount. The M_S values variate from 58.0 emu/g for sample $x = 0.0$ to 46.4 emu/g for sample $x = 0.5$. The M_r values range is also from 21.0 to 32.9 emu/g , and the range of variation of H_C is from 1132 to 5989 Oe .

Figure 6b reveals that the overall trends of M_S , M_r , and H_C are descending with increasing x , with some exceptions which will be described below.

As mentioned earlier, there are five positions for Fe^{3+} ferric ion in the BaM crystal structure, which are named 2a, 2b, 4f1, 4f2, and 12 k. The BaM unit cell included two molecular units of $\text{BaFe}_{12}\text{O}_{19}$, with a total of 24 ferric ions. Sites 2a, 2b, and 12 k have 2, 2, and 12 (16 in total) upward spin ferric ions, respectively, and sites 4f1 and 4f2 have 4 and 4 (8 in total) downward spin ones, respectively. Fe^{3+} ion has five unpaired electrons in the d orbital, and the magnetic moment of every single ion is equivalent to $5\mu_B$. Eight downward spins neutralize 8 spins from 16 upward spins, so the pure BaM unit cell has a net magnetization of $(16 - 8) * 5\mu_B = 40\mu_B$ and the net magnetic moment of one molecular unit of $\text{BaFe}_{12}\text{O}_{19}$ is half of this value $20\mu_B$ [13]. If the magnetic ions such as Mn^{2+} , whose magnetic moment is almost identical to ferric ions, are replaced at any of these five sites, no significant change will occur in the magnetization. If non-magnetic ions such as Ti^{4+} or Zn^{2+} are substituted instead of ferric ions at upward spin sites, the magnetization will be decreased, and if they are substituted at downward spin sites, the magnetization will be increased. Accordingly, the overall decreasing trend of M_S for substituted samples occurred due to the replacement of non-magnetic impurities, titanium, and zinc, instead of iron at different sites, owing to reducing the super-exchange interactions of Fe–O–Fe bonds. Despite this overall trend, sample $x = 0.3$ has a larger M_S than sample $x = 0.2$. This is explained by the results of the Rietveld refinement. On this basis, for sample $x = 0.3$, the sum of occupancy coefficients of Ti^{4+} and Zn^{2+} for downward spin sites (4f1 and 4f2) was the highest value among all samples. Therefore, in the unit cell of this sample ($x = 0.3$), upward spin ferric ions were less neutralized by downward spin ones, resulting in a slight increase in magnetization.

As the concentrations of non-magnetic impurities, titanium and zinc, increase, the M_r decreases due to the spin canting and reduction of magnetic collinearity. At low doping, H_C also decreased with increasing non-magnetic impurities. The reduction in coercivity is also associated with a reduction in the magnetocrystalline anisotropy of the BaM structure, and an easy axis is rotated from the c -axis to the basal plane. In general, anisotropy has a significant effect on the properties of Ba-hexaferrite, so that the magnetic specifications such as ferromagnetic resonance and MA quality are entirely dependent on anisotropy configuration [42, 43].

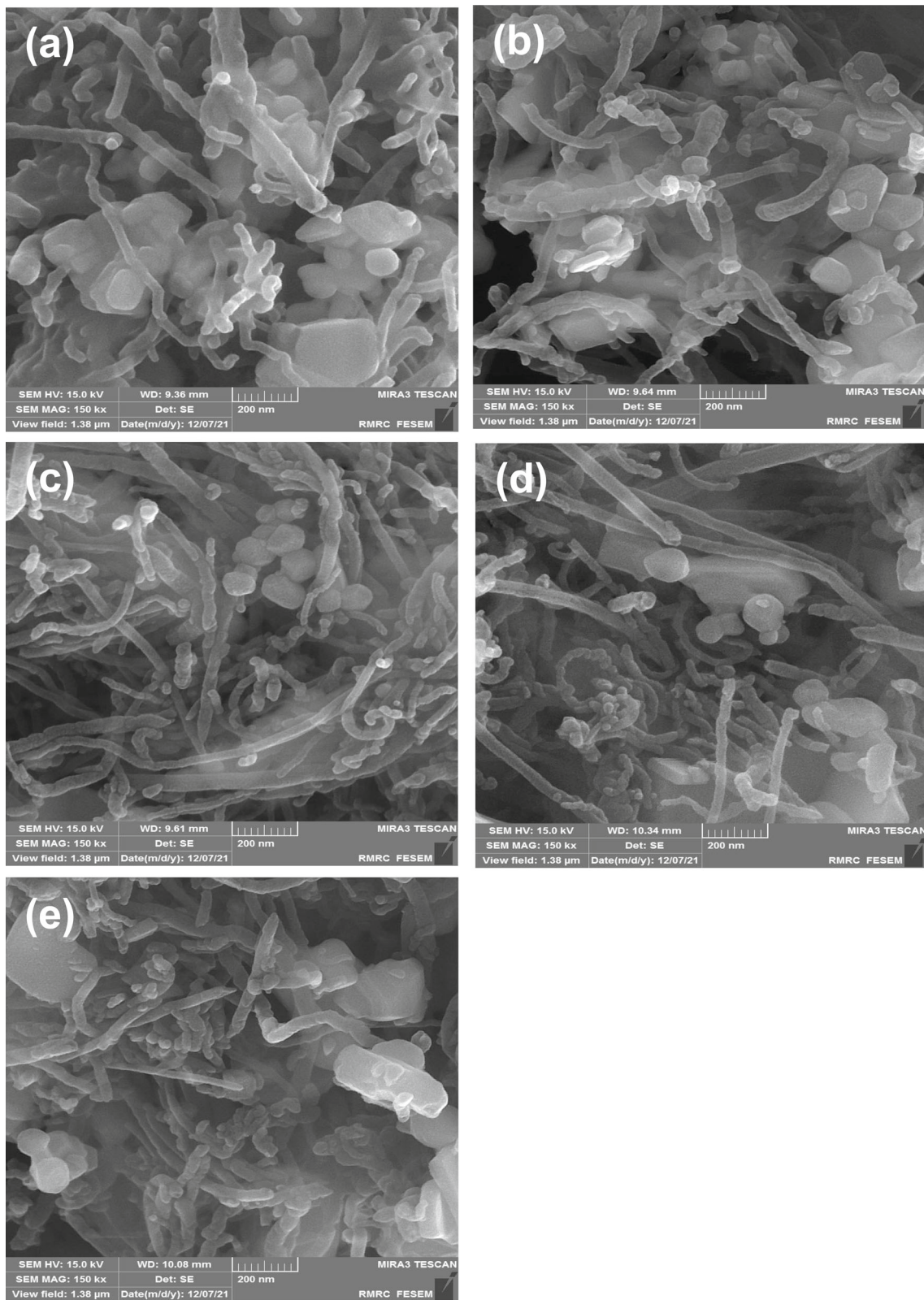


Fig. 3 The FE-SEM images with 150 Kx magnification of BaTi_{2x}Mn_xZn_xFe_{12-4x}/MWCNT nanocomposites at **a** $x = 0.0$, **b** $x = 0.2$, **c** $x = 0.3$, **d** $x = 0.4$, and **e** $x = 0.5$

Fig. 4 The TEM images of BaTi_{0.4}Mn_{0.2}Zn_{0.2}Fe_{11.2}/MWCNT nanocomposite. **a**, **b** Nanoparticles are seen sticking on the nanotubes, **c** nanoparticles and nanotubes are presented in the agglomerated form

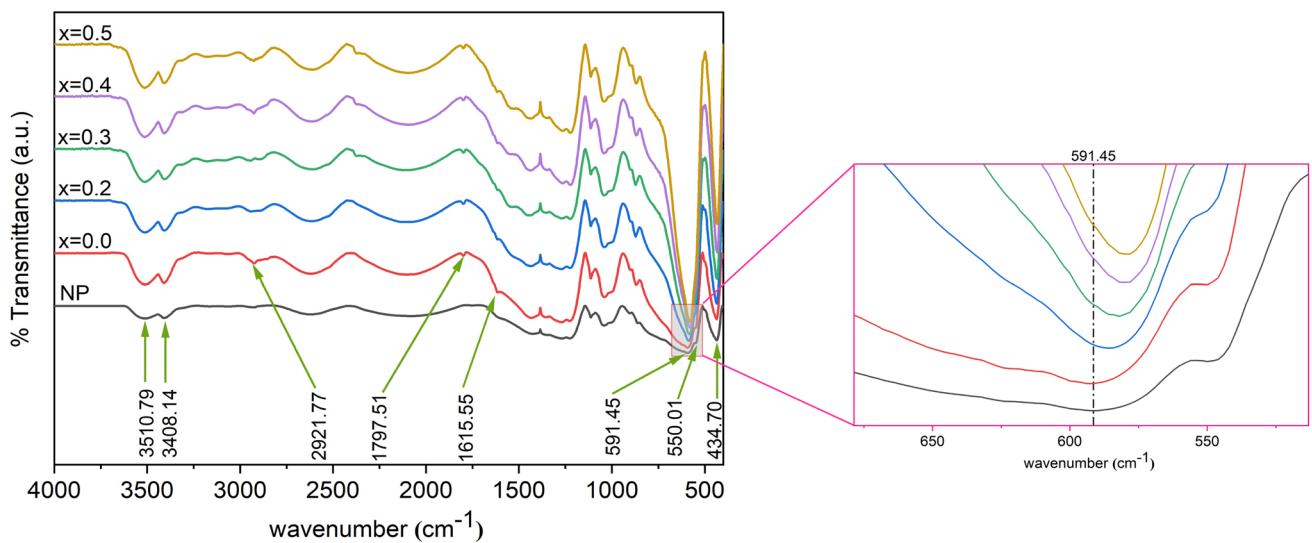
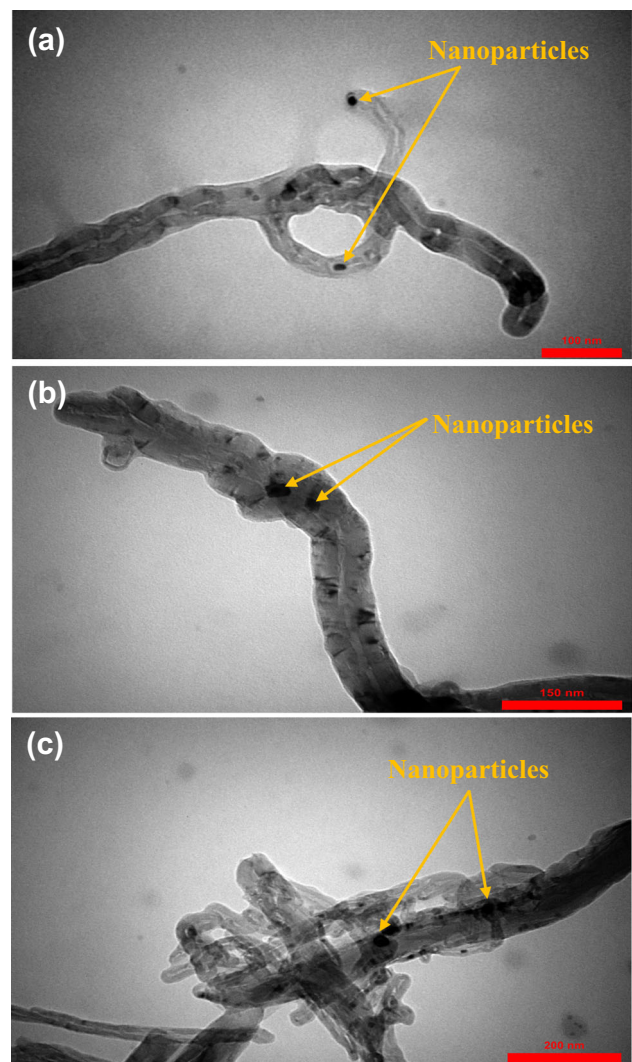
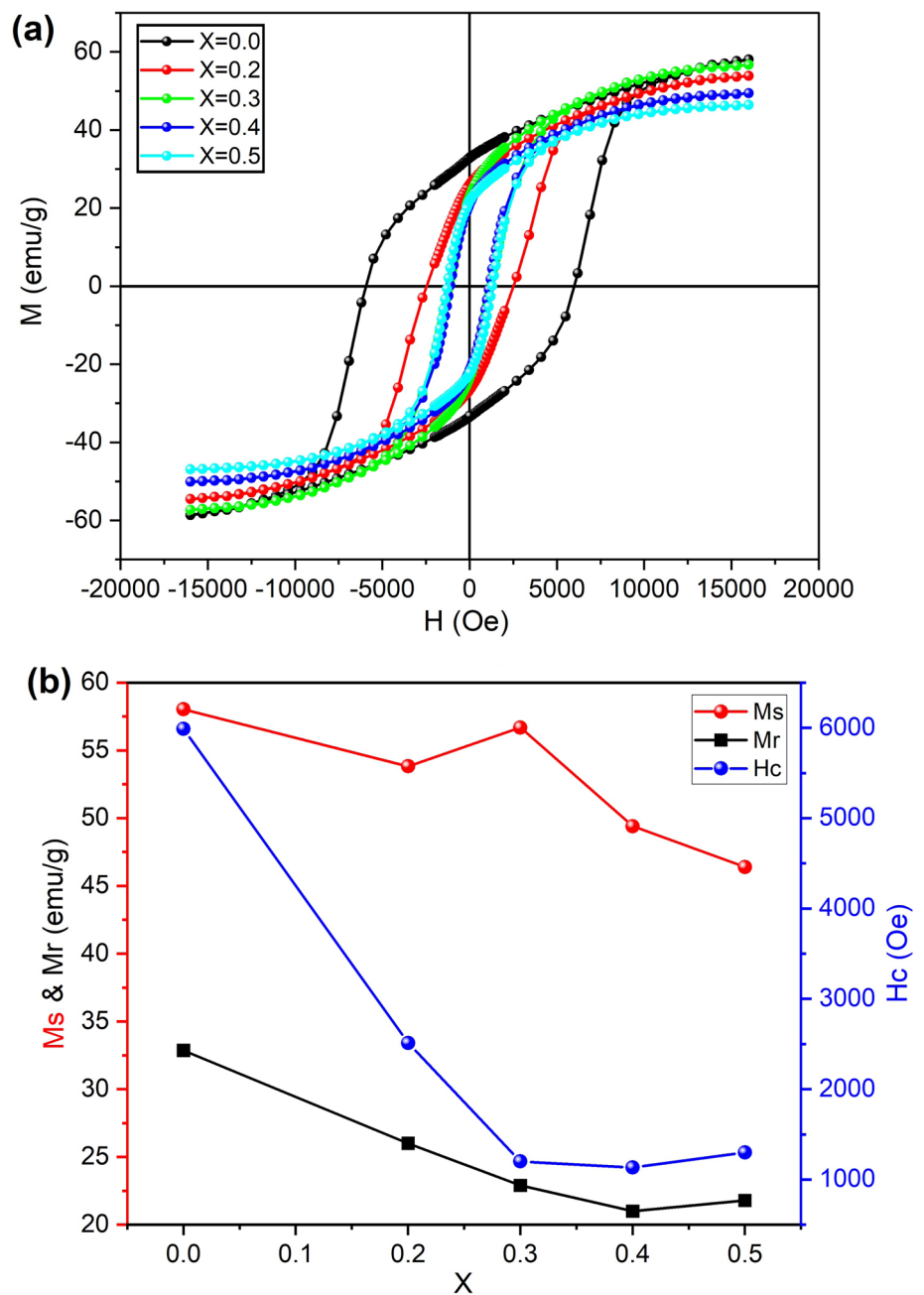


Fig. 5 The FTIR spectra for pure BaM (NP) and BaTi_{2x}Mn_xZn_xFe_{12-4x}/MWCNT nanocomposites for various concentrations of impurities (*x*)

Fig. 6 a The M–H hysteresis curves at room temperature for $\text{BaTi}_{2-x}\text{Mn}_x\text{Zn}_x\text{Fe}_{12-4x}/\text{MWCNT}$ samples with $x = 0.0, 0.2, 0.3, 0.4,$ and 0.5 . **b** M_S , M_r , and H_C values for different x



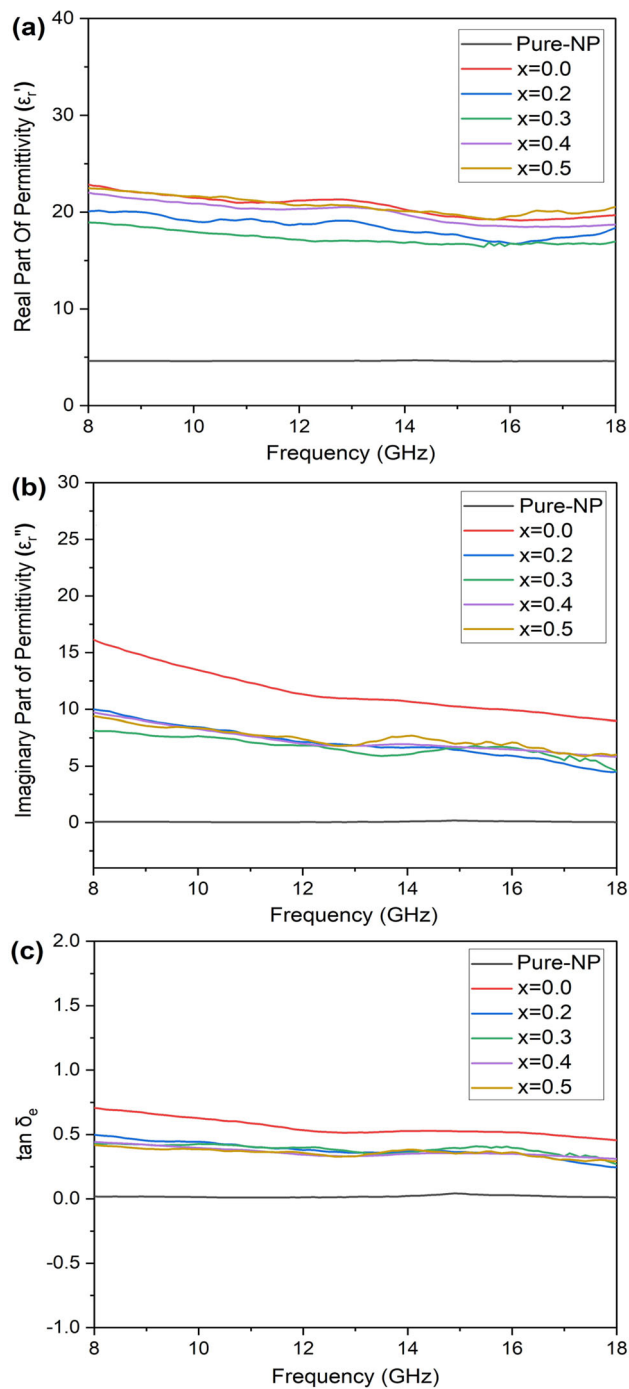
In general, some parameters such as morphology, particle size, ion substitution, crystal defects, strain, and interface structure change the performance, form, and width of the hysteresis curve. Therefore, changing the concentration of cations such as titanium, zinc, and manganese causes them to compete with each other and with iron for substitution in different sites [42].

3.3 Dielectric parameters and microwave absorption performance

In the following, it is necessary to describe some dielectric parameters related to microwave absorption properties. The complex permittivity and complex permeability can be represented as $\epsilon_r = |\epsilon_r|e^{i\delta_e}$ and $\mu_r = |\mu_r|e^{i\delta_m}$, respectively. In these relations, δ_e and δ_m are the electric and magnetic losses, respectively, which are equivalent to the tangent of the imaginary part divided by the real part. The loss tangent is defined as:

$$\tan \delta = \tan \delta_e + \tan \delta_m = \frac{\epsilon_r''}{\epsilon_r'} + \frac{\mu_r''}{\mu_r'} \quad (1)$$

Fig. 7 **a** The real part of permittivity (ϵ'_r), **b** the imaginary part of permittivity (ϵ''_r), and **c** electric loss tangent ($\tan \delta_e$) of pure BaFe₁₂O₁₉ nanoparticles (NP) and BaTi_{2x}Mn_xZn_xFe_{12-4x}/MWCNT nanocomposites with several amounts of x



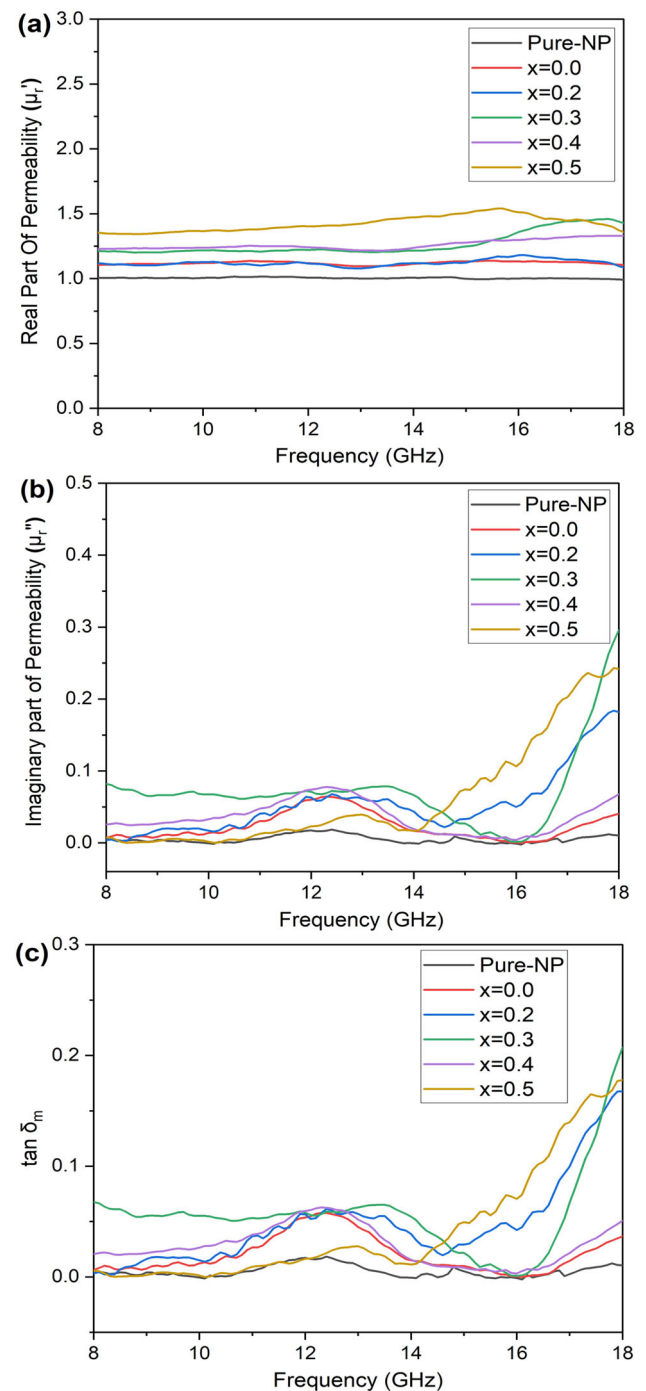
where ϵ'_r and ϵ''_r are the real and imaginary parts of the permittivity, respectively, and μ'_r and μ''_r are the real and imaginary parts of the permeability.

Figure 7 indicates ϵ'_r , ϵ''_r , and $\tan \delta_e$, and Fig. 8 shows μ'_r , μ''_r , and $\tan \delta_m$ versus the frequency for pure nanoparticles and nanocomposites with various amounts of impurities. These parameters have been calculated from scattering parameters in X and Ku microwave bands which are measured by the vector network analyzer. In general, the real parts, ϵ'_r and μ'_r , signify the storage capability, and the imaginary parts, ϵ''_r and μ''_r , indicate the dissipation of electrical and magnetic energy [44].

Figure 7 shows clearly that the addition of carbon nanotubes has increased ϵ'_r , ϵ''_r , and $\tan \delta_e$ of nanocomposites. This is due to the superior aspect ratio and high conductivity of MWCNTs, which is justified by the following equations [45].

$$\epsilon' = \epsilon_\infty + \frac{\epsilon_s - \epsilon_\infty}{1 + \omega^2 \tau^2} \tag{2}$$

Fig. 8 **a** The real part of permeability (μ_r'), **b** the imaginary part of permeability (μ_r''), and **c** magnetic loss tangent ($\tan \delta_m$) of pure BaFe₁₂O₁₉ nanoparticles (NP) and BaTi_{2x}Mn_xZn_xFe_{12-4x}/MWCNT nanocomposites with several amounts of x



$$\varepsilon'' = \frac{\varepsilon_s - \varepsilon_\infty}{1 + \omega^2 \tau^2} \omega \tau + \frac{\sigma}{\omega \varepsilon_0} \quad (3)$$

where ε_s , ε_∞ , and ε_0 are the static permittivity, high-frequency dielectric permittivity, and vacuum permittivity, respectively, τ is the relaxation time, ω is the angular frequency, and σ is the electrical conductivity.

Under the electromagnetic field, electrons in the composite gain the energy needed to pass through the BaM/MWCNT and BaM/BaM interfaces, forming the accumulation of spatial charges specific to the BaM/MWCNT composite, which can improve the dielectric loss of the composite [44]. These high values of electrical loss tangent provide the basis for improving the MA properties by enhancing the impedance matching, which will be described below.

In Fig. 8, some fluctuations in μ_r' , μ_r'' , and $\tan \delta_m$ can be observed, which is related to the natural resonance and eddy current loss when materials are exposed to electromagnetic radiation [25, 44, 46]. Also, as seen in the VSM analysis, the coercivity decreased

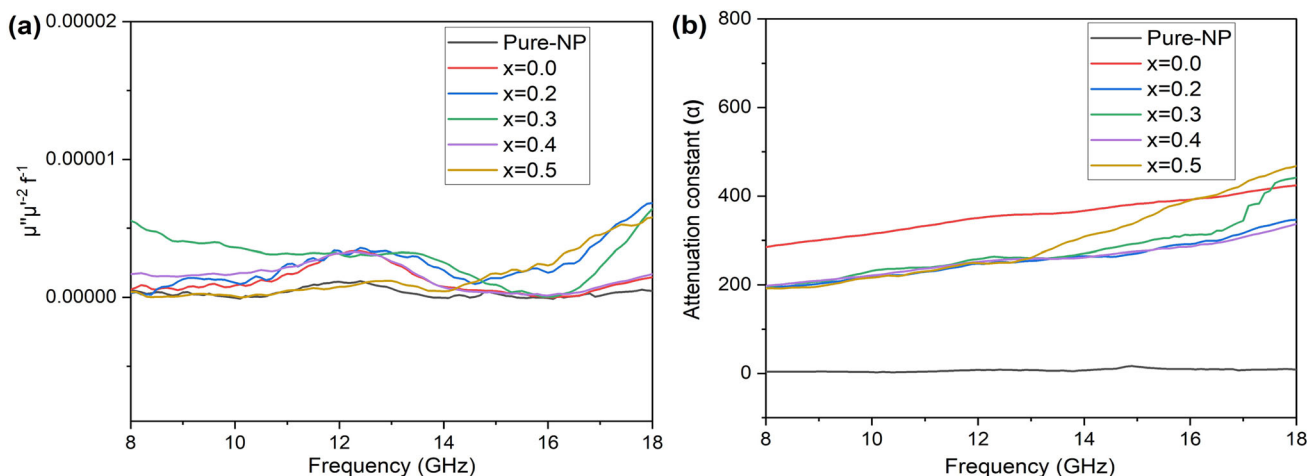


Fig. 9 **a** $C_0 = \mu''(\mu')^{-2} f^{-1}$ curve, **b** attenuation constant versus frequency for pure BaFe₁₂O₁₉ nanoparticles (NP) and BaTi_{2x}Mn_xZn_xFe_{12-4x}/MWCNT nanocomposites with several amounts of x

with increasing impurity concentration, and the samples became so-called softer. Therefore, the larger permeability of samples with larger x is not unexpected; in other words, the easier it is magnetized, the more permeable it is.

As it will be explained with the reasoning in the next few paragraphs, the relationship between resonance frequency (f_r) and the anisotropy field (H_a) is based on the following equation [19, 47].

$$f_r = \frac{\gamma}{2\pi} H_a \tag{4}$$

In this equation γ is the gyromagnetic ratio. The M-type ferrite’s imaginary part of permeability is written as follows [19]:

$$\mu'' = \frac{M_S}{2H_a\alpha} \tag{5}$$

where M_S is the saturation magnetization and α is the extinction coefficient. Using Eq. (4) we have:

$$\mu'' = \frac{\gamma M_S}{4\pi\alpha f_r} \tag{6}$$

So μ'' is related to f_r inversely. Now it is explained why in Fig. 8, μ''_r and $\tan \delta_m$ have grown at higher frequencies where μ'_r is almost constant. It is due to the fact that by increasing the frequency, we approach the natural magnetic resonance of the material, and the magnetic energy dissipation mechanisms become more active. In other words, in higher frequencies, > 14 GHz, the frequency of the orbital angular momentum and the frequency of the incoming electromagnetic wave are more coordinated. Therefore the wave is trapped and absorbed in the matter. Since the substituted samples have a lower f_r due to the smaller H_a , the growth of μ''_r and $\tan \delta_m$ starts from lower frequencies, proportional to the concentrations of impurities.

Also, the μ''_r peaks observed at around 12 GHz correspond to the eddy current loss and the synergistic interactions amid ferrite nanoparticles and MWCNTs [44, 46]; this can be explained by Eq. (7). The C_0 remains constant throughout the frequency band if the magnetic loss is just included with the eddy current loss [46, 48]. But some fluctuations which can be seen on the C_0 curve (see Fig. 9) prove that there is some other loss mechanism than eddy current in BaM-MWCNT composites. It means that combining ferrite nanoparticles with MWCNTs has not only improved the dielectric loss but also developed magnetic loss and enhanced MA performance [47].

$$C_0 = \mu''(\mu')^{-2} f^{-1} \tag{7}$$

Figure 9b indicates the attenuation constant (α) curves of the pure nanoparticles and nanocomposites. This constant, given by Eq. (8), is an estimate of electromagnetic energy dissipation in the matter [44, 49]. Pure composite and their doped one have a higher attenuation constant than pure BaM due to higher dielectric and magnetic loss [50]. Meanwhile, for the specimens $x = 0.3$ and $x = 0.5$ in the frequency range higher than 13 GHz, the synergy between carbon nanotubes and impurities in increasing dielectric and magnetic losses has led to an increase in α .

$$\alpha = \frac{\sqrt{2\pi}f}{C} \sqrt{(\mu''_r\epsilon''_r - \mu'_r\epsilon'_r) + \sqrt{(\mu''_r\epsilon''_r - \mu'_r\epsilon'_r)^2 + (\mu'_r\epsilon''_r + \mu''_r\epsilon'_r)^2}} \tag{8}$$

The MWCNT plays a significant role in enhancing microwave attenuation. By synthesizing a nanocomposite of the MWCNT-ferrite NPs network in the paraffin medium, due to the existence of spatial charge accumulation in BaM/MWCNT interfaces, the

dielectric loss is increased. Another advantage of this network is the creation of the multiple scattering process of microwave, thus improving the microwave attenuation performance. In addition, the stray magnetic flux lines radiated from magnetic elements of the nanoparticles can propagate into the non-magnetic void or paraffin space among the MWCNTs [51–53]. This leads to more magnetic loss, better impedance matching, and further attenuation.

In the case of the interaction of electromagnetic waves with targets, the essential condition for achieving the minimum reflection (maximum absorption) is impedance matching. The electromagnetic wave must have the appropriate requirements to enter the absorber. To meet this purpose, the intrinsic impedance of the absorber (Z_{in}) must stay as near as feasible to the intrinsic impedance of surrounding free space (Z_0). It means the impedance matching condition is $|Z_{in}/Z_0| \approx 1$. In this condition, most of the waves enter the matter; then, based on various mechanisms of microwave absorption, energy is dissipated within it. The input impedance, which depends on the incident frequency, is calculated from Eq. (9) [54].

$$Z_{in} = Z_0 \sqrt{\frac{\mu_r}{\epsilon_r}} \tanh \left[j \left(\frac{2\pi f d}{C} \right) \sqrt{\mu_r \epsilon_r} \right] \quad (9)$$

where $Z_0 = (\mu_0/\epsilon_0)^{1/2} = 377\Omega$ is the impedance of free space, f is the input electromagnetic wave frequency, d is the thickness of the absorber piece, and C is the speed of light in a vacuum. A reflective metal plate is placed behind the absorber piece. The more the reflected wave from the back metal plate is attenuated, the better performance of the absorbing material. The amount of reflection loss in terms of absorbance (A), reflectance (R), and impedance is calculated based on the following equation [55].

$$RL(dB) = 10 \log(1 - A) = 10 \log(R) = 20 \log \left| \frac{Z_{in} - Z_0}{Z_{in} + Z_0} \right| \quad (10)$$

The conventional limit of $RL = -10$ is equivalent to 90% absorption. Those materials having an RL lower than or equal to this limit are appropriate for MA applications. The bandwidth for the RL below -10 dB is essential, and the wider it is, the more applicable.

Here, 2D and 3D graphs were used to describe the impedance matching and reflection loss performance in the X and Ku microwave bands for pure nanoparticles and $BaTi_{2-x}Mn_xZn_xFe_{12-4x}/MWCNT$ nanocomposites with different concentrations of dopants in the thickness range of 0.8–1.6 mm (see Figs. 10, 11, and 12). It is clearly observed that adding impurities and carbon nanotubes improved the RL and increased the absorption in these two well-known frequency bands. There are multiple reasons for this effect; first of all, the presence of MWCNTs has resulted in better impedance matching conditions. In this case, multiple scatterings within the matter due to higher interfaces are one of the reasons for increasing the reflection loss [17, 56]. The comparison of Fig. 10a with b for nanoparticles and pure nanocomposites reveals the effect of MWCNTs addition alone.

Another significant factor in increasing the MA at the frequency range of 8–18 GHz is the ferromagnetic resonance (f_r) shift from higher frequencies to this range by adding Ti^{4+} , Mn^{2+} , and Zn^{2+} cations. By definition, ferromagnetic resonance means the co-frequency of the precession of an orbital angular momentum with the applied magnetic field H . According to Eq. (4), f_r is expressed in terms of H_C as: $f_r = \frac{\gamma}{2\pi} H_a$. Anisotropy, which is an intra-structural field, tends to direct the magnetization along the easy axis; consequently, the anisotropy field is proportional to the coercivity [36]. Hence, the shift down of resonance frequency corresponds to the decreasing of coercivity, which occurred due to the addition of impurities and increasing them. Figure 11a shows that for a given thickness ($d = 1.1$ mm), as the concentration of impurities is increased from $x = 0.0$ to $x = 0.5$, the resonance frequency reduces quite proportionally. Figure 11b indicates the normalized impedance matching curve at the thickness of 1.1 mm. As mentioned, the closer the Z_{in}/Z_0 value is to 1, the better the impedance matching is and the most appropriate conditions to enter the wave into the matter. The specimen with $x = 0.5$ has maximum normalized impedance matching (equal to 0.95) as it has the minimum of RL in this thickness (Fig. 11a). In other thicknesses, the higher normalized impedance matching is seen too; for example, at the thickness of 0.9 mm, the sample $x = 0.3$ has $Z_{in}/Z_0 = 1.004$ which is the highest among all. In Eq. (9), based on the condition of the hyperbolic tangent function, i.e., $\tanh \left[j \left(\frac{2\pi f d}{C} \right) \sqrt{\mu_r \epsilon_r} \right]$, impedance matching would be improved when the magnetic contribution matched the dielectric contribution [55, 57].

Based on Figs. 10, 11, and 12, it turns out that the best reflection loss is taken place for the samples $x = 0.4$ and $x = 0.5$. The lowest RL belongs to the sample $x = 0.4$, which has reached -31.5 dB at the thickness of only 0.9 mm, and it is the lowest value among all samples and in all thicknesses. The best maximum bandwidth (BW_{max}) of 3.89 GHz was achieved for the sample $x = 0.5$ at the thickness of 0.9 mm. The entire X and Ku frequency bands are covered by a thickness change of only 0.8 mm ($d = 0.8$ –1.6 mm). It is great to obtain these appropriate values for RL_{min} and BW_{max} in such a small thickness and narrow thickness range.

Given the above, this nanocomposite is recommended for use in MA applications where the mass and volume considerations of the absorber are of distinct prominence. For example, in the case of the stealth of aircraft and UAVs, weight consideration is an essential issue, so the coating of this equipment with such a thin layer would be precious.

Table 2 shows the comparison of the performance of some composite absorbers reported in recent years. In none of the similar works, the achievement of RL_{min} to a value of about -31.5 dB in such a small thickness (0.9 mm) has not occurred. In many papers on microwave absorption, it is observed that the RL_{min} is significantly weakened by reducing the absorber thickness even by 0.1 mm as can be checked in some references in Table 2.

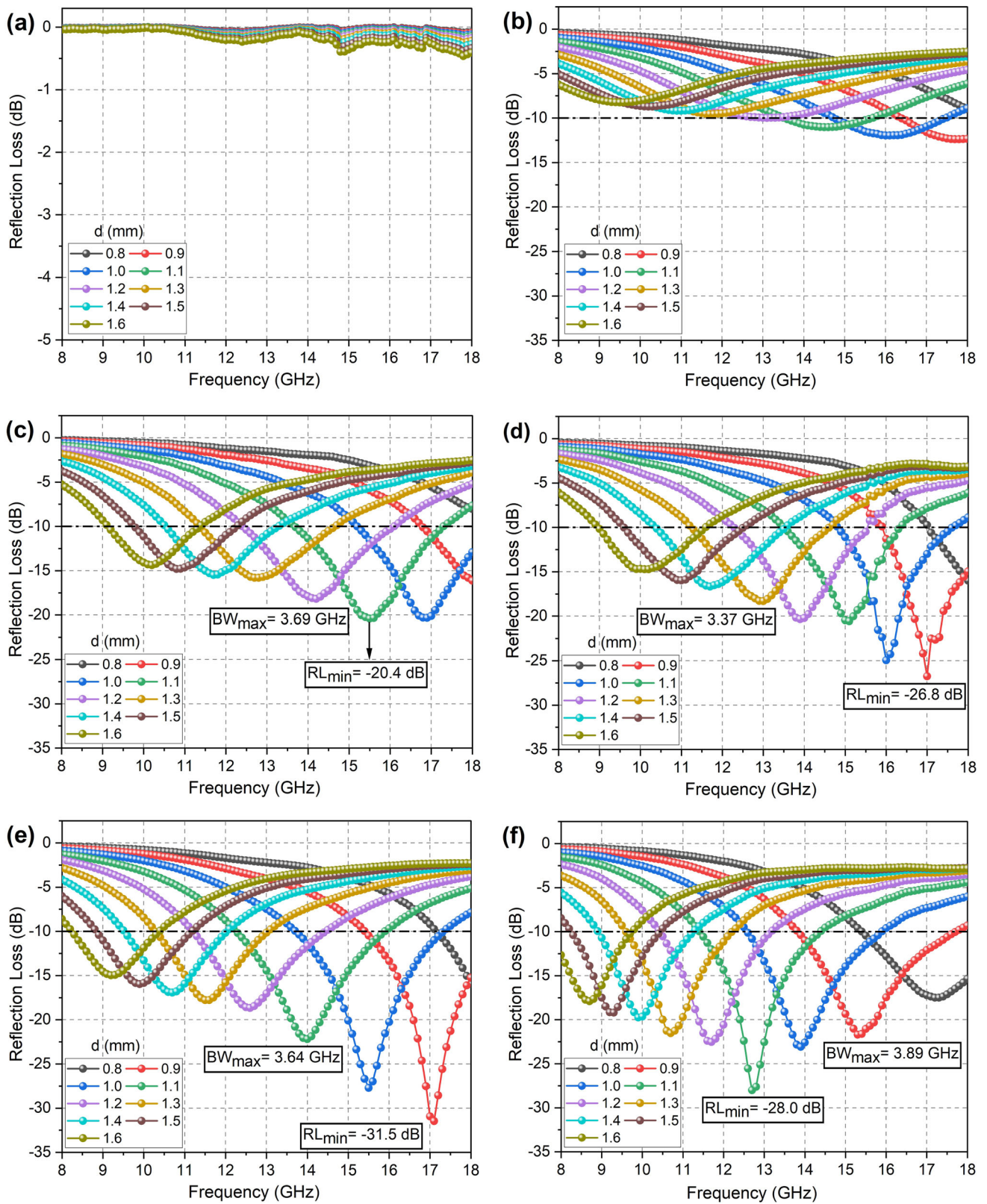


Fig. 10 The reflection loss vs. frequency for **a** pure $BaFe_{12}O_{19}$ nanoparticles and $BaTi_{2-x}Mn_xZn_xFe_{12-4x}/MWCNT$ nanocomposites for various concentrations of impurities (x): **b** $x = 0.0$, **c** $x = 0.2$, **d** $x = 0.3$, **e** $x = 0.4$, and **f** $x = 0.5$

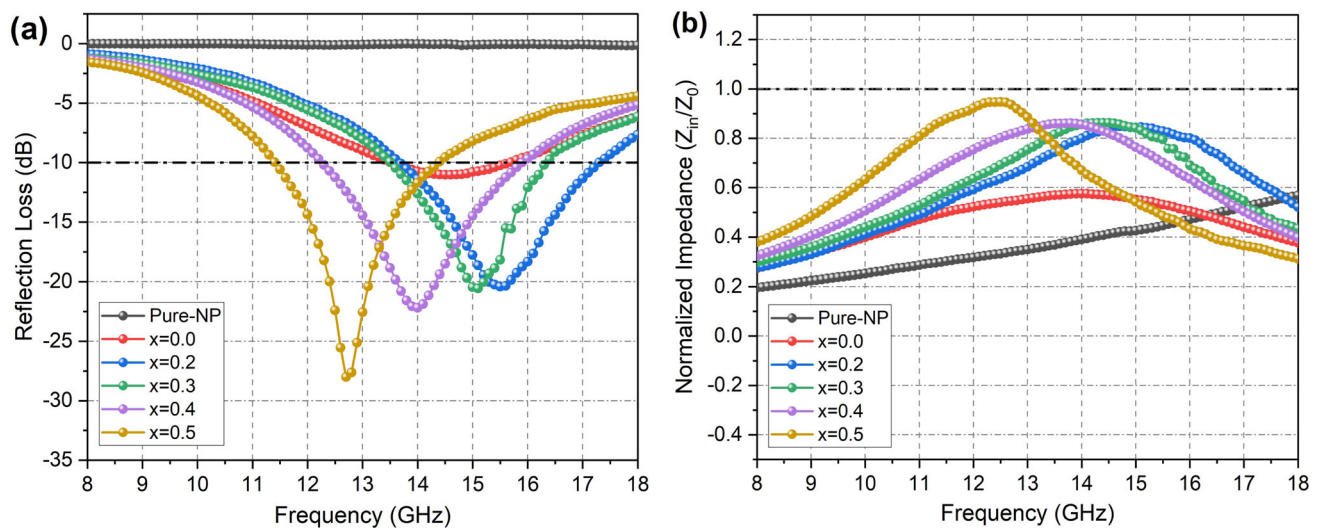


Fig. 11 **a** The reflection loss versus frequency, **b** Normalized impedance (Z_{in}/Z_0), for pure $BaFe_{12}O_{19}$ nanoparticles and $BaTi_{2x}Mn_xZn_xFe_{12-4x}/MWCNT$ nanocomposites for various concentrations of impurities (x) at the thickness of 1.1 mm

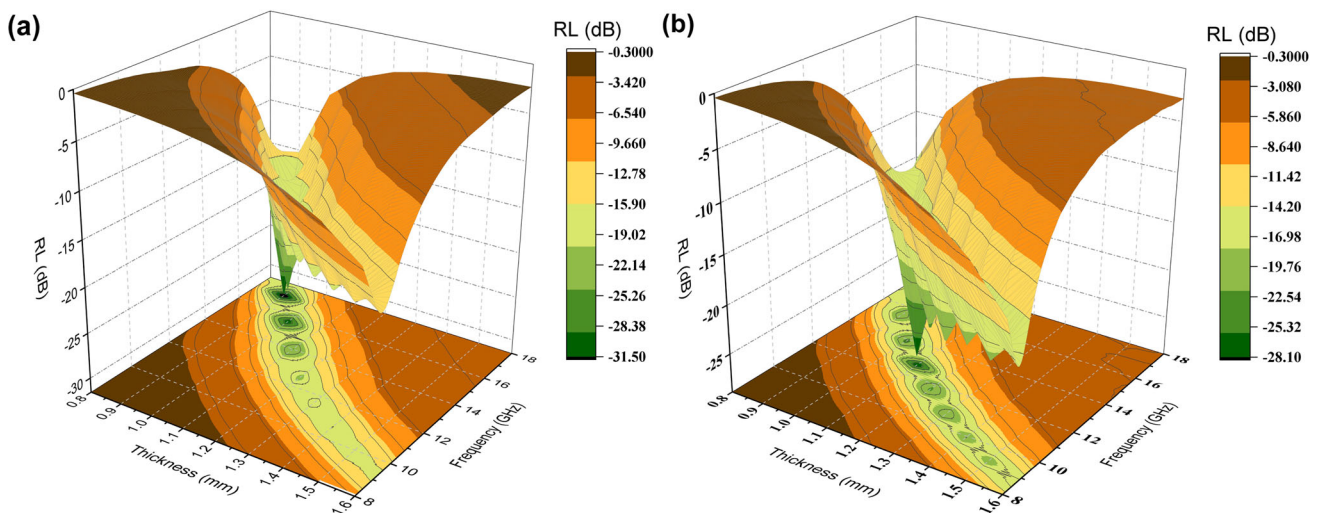


Fig. 12 The 3D RL color maps of $BaTi_{2x}Mn_xZn_xFe_{12-4x}/MWCNT$ nanocomposites for **a** $x = 0.4$ and **b** $x = 0.5$

4 Conclusions

Substituted hexaferrite nanoparticles, $BaTi_{2x}Mn_xZn_xFe_{12-4x}O_{19}$ with various amounts of x were synthesized using the modified sol-gel auto-combustion technique and then compounded with COOH-functionalized MWCNT to make nanocomposites. Refined XRD and FTIR diagrams proved the forming of the M-type hexaferrite crystal structure. It was determined the tendency of dopants to replace instead of ferric ions in different crystallographic sites. FE-SEM and TEM were used to study morphology. The confirmation of nanoparticle formation and homogeneous configuration of nanoparticles and nanotubes were obtained. The M-H hysteresis curves exhibited that by increasing the concentration of impurities, the coercivity and saturation magnetization decreased owing to the reduction of anisotropy field and super-exchange interactions. However, there were a few exceptions explained by Rietveld refinement outcomes. Consequently, according to the anisotropy field decreasing and the dependency of resonance frequency on it, this frequency shifted from unwanted (in this work) higher ones to the lower values in X and Ku bands, as seen in RL graphs. RL_{min} reached -31.5 dB at the thickness of just 0.9 mm for the sample $x = 0.4$, and BW_{max} attained 3.89 GHz for sample $x = 0.5$. The entire X and Ku bandwidth were covered by the thickness change of only 0.8 mm (0.8–1.6 mm). Based on the above, this effective thin nanocomposite is suitable for applications of MA in which weight and volume considerations are of particular importance such as stealth and EMI shielding applications.

Table 2 Comparison of the absorbing properties of some composite absorbers reported in recent years

Composite absorber	Thickness (mm)	RL _{min} (dB)	Corresponding frequency (GHz)	Bandwidth (GHz)	References
BaFe ₁₂ O ₁₉ @ZnFe ₂ O ₄ /MWCNTs	2.5	− 42.3	8.2	~2.5	[58]
RGO/MWCNTs/ZnFe ₂ O ₄	5.0	− 23.8	4.4	2.6	[59]
Ni _{0.4} Cu _{0.6} Fe ₂ O ₄ -MWCNT	1.3	− 28.43	~ 14.5	3.7	[46]
RGO/Co _{0.5} Zr _{0.5} Fe ₂ O ₄	5.0	− 31.89	4.2	4.0	[60]
CF@CoFe ₂ O ₄ @MnO ₂	1.5	− 34	14.5	5	[61]
BaFe ₁₂ O ₁₉ /CNT	1.5	− 29.7	15.78	3.2	[62]
SrFe _{9.8} Co _{1.1} Ti _{1.1} O ₁₉ -epoxy	1.5	− 30.4	13.5	>5.5	[17]
ZnFe ₂ O ₄ /GNs (10 wt%)	1.3	− 34.56	~ 15	4.05	[63]
CCF-Fe ₃ O ₄	1.67	− 56.8	10.9	7.1	[64]
BaTi _{0.8} Mn _{0.4} Zn _{0.4} Fe _{10.4} /MWCNT	0.9	− 31.5	17.1	3.64	This work

References

1. Y. Chen, H. Bin Zhang, Y. Yang, M. Wang, A. Cao, Z.Z. Yu, *Adv. Funct. Mater.* **26**, 447 (2016). <https://doi.org/10.1002/adfm.201503782>
2. A. Iqbal, F. Shahzad, K. Hantanasirisakul, M.K. Kim, J. Kwon, J. Hong, H. Kim, D. Kim, Y. Gogotsi, C.M. Koo, *Science* **369**, 446 (2020). <https://doi.org/10.1126/science.aba7977>
3. J. Li, Z. Xu, T. Li, D. Zhi, Y. Chen, Q. Lu, J. Wang, Q. Liu, F. Meng, *Compos. Part B Eng.* **231**, 109565 (2022). <https://doi.org/10.1016/j.compositesb.2021.109565>
4. W. Liu, L. Liu, G. Ji, D. Li, Y. Zhang, Y. Du, A.C.S. Sustain, *Chem. Eng.* **5**, 7961 (2017). <https://doi.org/10.1021/acssuschemeng.7b01514>
5. Q. Hu, R. Yang, Z. Mo, D. Lu, L. Yang, Z. He, H. Zhu, Z. Tang, X. Gui, *Carbon N. Y.* **153**, 737 (2019). <https://doi.org/10.1016/j.carbon.2019.07.077>
6. F. Gan, Q. Yao, L. Cheng, L. Zhang, Q. Liang, J. Guo, M. Wang, H. Zhou, Y. Zhong, *J. Alloys Compd.* **897**, 162964 (2022). <https://doi.org/10.1016/j.jallcom.2021.162964>
7. J. Tao, J. Zhou, Z. Yao, Z. Jiao, B. Wei, R. Tan, Z. Li, *Carbon N. Y.* **172**, 542 (2021). <https://doi.org/10.1016/j.carbon.2020.10.062>
8. R. Shu, J. Zhang, C. Guo, Y. Wu, Z. Wan, J. Shi, Y. Liu, M. Zheng, *Chem. Eng. J.* **384**, 123266 (2020). <https://doi.org/10.1016/j.cej.2019.123266>
9. J. Liu, Y. Duan, L. Song, J. Hu, Y. Zeng, *Compos. Sci. Technol.* **182**, 107780 (2019). <https://doi.org/10.1016/j.compscitech.2019.107780>
10. J. Mahapatro, S. Agrawal, *J. Alloys Compd.* **907**, 164405 (2022). <https://doi.org/10.1016/j.jallcom.2022.164405>
11. S. Jiao, M. Wu, X. Yu, H. Zhang, *Adv. Eng. Mater.* **22**, 1 (2020). <https://doi.org/10.1002/adem.201901299>
12. X. Li, L. Wang, W. You, L. Xing, X. Yu, Y. Li, R. Che, *Nanoscale* **11**, 2694 (2019). <https://doi.org/10.1039/C8NR08601J>
13. R.C. Pullar, *Prog. Mater. Sci.* **57**, 1191 (2012). <https://doi.org/10.1016/j.pmatsci.2012.04.001>
14. F. Hu, H. Nan, M. Wang, Y. Lin, H. Yang, Y. Qiu, B. Wen, *Ceram. Int.* **47**, 16579 (2021). <https://doi.org/10.1016/j.ceramint.2021.02.229>
15. S. Goel, M. Bala, A. Garg, V.D. Shivling, S. Tyagi, *Mater. Today Proc.* **28**, 1753–1758 (2020). <https://doi.org/10.1016/j.matpr.2020.05.157>
16. J. Liu, X. Feng, S. Wu, P. Zhou, J. Huang, H. Li, T. Liang, *J. Alloys Compd.* **892**, 162207 (2022). <https://doi.org/10.1016/j.jallcom.2021.162207>
17. J. Yoo, Y. Kang, *J. Magn. Magn. Mater.* **513**, 167075 (2020). <https://doi.org/10.1016/j.jmmm.2020.167075>
18. M. Sharma, S.C. Kashyap, *Ceram. Int.* **45**, 11226 (2019). <https://doi.org/10.1016/j.ceramint.2019.02.136>
19. H. Nikmanesh, M. Moradi, G.H. Bordbar, R. Sham Aslam, *J. Alloys Compd.* **708**, 99 (2017). <https://doi.org/10.1016/j.jallcom.2017.02.308>
20. G. Feng, W. Zhou, H. Deng, D. Chen, Y. Qing, C. Wang, F. Luo, D. Zhu, Z. Huang, Y. Zhou, *Ceram. Int.* **45**, 13859 (2019). <https://doi.org/10.1016/j.ceramint.2019.04.083>
21. M. Rostami, M. Moradi, R.S. Alam, R. Mardani, *J. Electron. Mater.* **45**, 4154 (2016). <https://doi.org/10.1007/s11664-016-4635-x>
22. A.R. Kagdi, N.P. Solanki, F.E. Carvalho, S.S. Meena, P. Bhatt, R.C. Pullar, R.B. Jotania, *J. Alloys Compd.* **741**, 377 (2018). <https://doi.org/10.1016/j.jallcom.2018.01.092>
23. H. Li, L. Zheng, D. Deng, X. Yi, X. Zhang, X. Luo, Y. Wu, W. Luo, M. Zhang, *J. Alloys Compd.* **862**, 158638 (2021). <https://doi.org/10.1016/j.jallcom.2021.158638>
24. V.D. Phadtare, V.G. Parale, G.K. Kulkarni, H.H. Park, V.R. Puri, *J. Alloys Compd.* **765**, 878 (2018). <https://doi.org/10.1016/j.jallcom.2018.06.299>
25. M. Rostami, M. Jafarpour, M.H. Majles Ara, *J. Alloys Compd.* **872**, 159656 (2021). <https://doi.org/10.1016/j.jallcom.2021.159656>
26. W. Widanarto, M. Effendi, S.K. Ghoshal, C. Kurniawan, E. Handoko, M. Alaydrus, *Curr. Appl. Phys.* **20**, 638 (2020). <https://doi.org/10.1016/j.cap.2020.02.019>
27. G. Sriramulu, N. Maramu, B.R. Reddy, A. Kandasami, S. Katlakunta, *Mater. Res. Bull.* **149**, 111732 (2022). <https://doi.org/10.1016/j.cap.2020.02.019>
28. R.B. Jotania, R.B. Khomane, C.C. Chauhan, S.K. Menon, B.D. Kulkarni, *J. Magn. Magn. Mater.* **320**, 1095 (2008). <https://doi.org/10.1016/j.jmmm.2007.10.032>
29. A. Garg, S. Goel, A.K. Dixit, M.K. Pandey, N. Kumari, S. Tyagi, *Mater. Chem. Phys.* **257**, 123771 (2021). <https://doi.org/10.1016/j.matchemphys.2020.123771>
30. G.R. Gordani, A. Ghasemi, A. Saidi, *Ceram. Int.* **40**, 4945 (2014). <https://doi.org/10.1016/j.ceramint.2013.10.096>
31. H. Sözeri, Z. Mehmedi, H. Kavas, A. Baykal, *Ceram. Int.* **41**, 9602 (2015). <https://doi.org/10.1016/j.ceramint.2015.04.022>
32. H. Sözeri, H. Deligöz, H. Kavas, A. Baykal, *Ceram. Int.* **40**, 8645 (2014). <https://doi.org/10.1016/j.ceramint.2014.01.082>
33. K.K. Ji, Y. Li, M.S. Cao, *J. Mater. Sci. Mater. Electron.* **27**, 5128 (2016). <https://doi.org/10.1007/s10854-016-4404-x>
34. S. Zhang, C. Meng, L. Zhang, S. Yuan, H. Luo, S. Liu, H. Chang, *J. Magn. Magn. Mater.* **513**, 167076 (2020). <https://doi.org/10.1016/j.jmmm.2020.167076>
35. P. Wartewig, M.K. Krause, P. Esquinazi, S. Rösler, R. Sonntag, *J. Magn. Magn. Mater.* **192**, 83 (1999). [https://doi.org/10.1016/S0304-8853\(98\)00382-5](https://doi.org/10.1016/S0304-8853(98)00382-5)
36. M. Elansary, M. Belaiche, C. Ahmani Ferdi, E. Iffer, I. Bsoul, *RSC Adv.* **10**, 25239 (2020). <https://doi.org/10.1039/d0ra04722h>
37. R.S. Alam, M. Moradi, M. Rostami, H. Nikmanesh, R. Moayedi, Y. Bai, *J. Magn. Magn. Mater.* **381**, 1 (2015). <https://doi.org/10.1016/j.jmmm.2014.12.059>

38. M.J.S.S. Seyyed Afghahi, R. Peymanfar, S. Javanshir, Y. Atassi, P. Leukot, *Essent. Fat. Acids* **115**, 60 (2016). <https://doi.org/10.1016/j.jmmm.2016.09.082>
39. J. Ke, X. Li, F. Wang, S. Jiang, M. Kang, J. Wang, Q. Li, Z. Wang, *RSC Adv.* **7**, 28841 (2017). <https://doi.org/10.1039/c7ra04215a>
40. B. Zeynizadeh, E. Gholamiyan, M. Gilanizadeh, *Curr. Chem. Lett.* **7**, 121 (2018). <https://doi.org/10.5267/j.ccl.2018.11.001>
41. D. Hudiyanti, M.F. Al khafiz, K. Anam, P. Siahaan, L. Suyati, *Open Chem.* **19**, 358 (2021). <https://doi.org/10.1515/chem-2021-0036>
42. H. Nikmanesh, S. Hoghoghifard, B. Hadi-Sichani, M. Moradi, *Mater. Sci. Eng. B Solid State Mater. Adv. Technol.* **262**, 114796 (2020). <https://doi.org/10.1016/j.mseb.2020.114796>
43. J.M.D. Coey, *Magnetism and Magnetic Materials* (Cambridge University Press, New York, 2010)
44. Y.Y. Wang, W. Song Yang, J. Sun, K. Dai, D.X. Yan, Z.M. Li, *J. Mater. Sci. Technol.* **102**, 115 (2022). <https://doi.org/10.1016/j.jmst.2021.06.032>
45. C. Wang, J. Li, S. Guo, *Compos. Part A Appl. Sci. Manuf.* **125**, 105522 (2019). <https://doi.org/10.1016/j.compositesa.2019.105522>
46. M. Rostami, M.H. Majlesara, *Ceram. Int.* **45**, 7606 (2019). <https://doi.org/10.1016/j.ceramint.2019.01.056>
47. R. Shams Alam, M. Moradi, H. Nikmanesh, J. Ventura, M. Rostami, *J. Magn. Magn. Mater.* **402**, 20 (2016). <https://doi.org/10.1016/j.jmmm.2015.11.038>
48. G. Wang, Z. Gao, G. Wan, S. Lin, P. Yang, Y. Qin, *Nano Res.* **7**, 704 (2014). <https://doi.org/10.1007/s12274-014-0432-0>
49. B. Zhao, G. Shao, B. Fan, W. Zhao, R. Zhang, *Phys. Chem. Chem. Phys.* **17**, 2531 (2015). <https://doi.org/10.1039/C4CP05031B>
50. R. Shu, Z. Wan, J. Zhang, Y. Wu, J. Shi, *Compos. Sci. Technol.* **210**, 108818 (2021). <https://doi.org/10.1016/j.compscitech.2021.108818>
51. Z. Wu, K. Pei, L. Xing, X. Yu, W. You, R. Che, *Adv. Funct. Mater.* **29**, 1 (2019). <https://doi.org/10.1002/adfm.201901448>
52. Y.F. Zhu, L. Zhang, T. Natsuki, Y.Q. Fu, Q.Q. Ni, *A.C.S. Appl. Mater. Interfaces* **4**, 2101 (2012). <https://doi.org/10.1021/am300069x>
53. Q. Liu, Q. Cao, H. Bi, C. Liang, K. Yuan, W. She, Y. Yang, R. Che, *Adv. Mater.* **28**, 486 (2016). <https://doi.org/10.1002/adma.201503149>
54. Y. Naito, K. Suetake, *IEEE Trans. Microw. Theory Tech.* **19**, 65 (1971). <https://doi.org/10.1109/TMTT.1971.1127446>
55. Z. Wu, H.W. Cheng, C. Jin, B. Yang, C. Xu, K. Pei, H. Zhang, Z. Yang, R. Che, *Adv. Mater.* **34**, 1 (2022). <https://doi.org/10.1002/adma.202107538>
56. Y. Cao, A. Mustafa Mohamed, A. Sharifi, M. Niaz Akhtar, *J. Magn. Magn. Mater.* **524**, 167653 (2021). <https://doi.org/10.1016/j.jmmm.2020.167653>
57. R.C. Che, C.Y. Zhi, C.Y. Liang, X.G. Zhou, *Appl. Phys. Lett.* **88**, 1 (2006). <https://doi.org/10.1063/1.2165276>
58. M. Lu, J. Wang, X. Su, Q. Wu, T. Yan, X. Zhang, *Mater. Lett.* **253**, 46 (2019). <https://doi.org/10.1016/j.matlet.2019.06.012>
59. R. Shu, W. Li, X. Zhou, D. Tian, G. Zhang, Y. Gan, J. Shi, J. He, *J. Alloys Compd.* **743**, 163 (2018). <https://doi.org/10.1016/j.jallcom.2018.02.016>
60. S. Gunasekaran, K. Thanrasu, A. Manikandan, M. Durka, A. Dinesh, S. Anand, S. Shankar, Y. Slimani, M.A. Almessiere, A. Baykal, *Phys. B Condens. Matter* **605**, 412784 (2021). <https://doi.org/10.1016/j.physb.2020.412784>
61. A. Feng, T. Hou, Z. Jia, G. Wu, *RSC Adv.* **10**, 10510 (2020). <https://doi.org/10.1039/C9RA10327A>
62. A. Afzali, V. Mottaghitalab, S.S. Seyyed Afghahi, M. Jafarian, Y. Atassi, *J. Magn. Magn. Mater.* **442**, 224 (2017). <https://doi.org/10.1016/j.jmmm.2017.06.119>
63. J. Zhou, B. Wei, M. Wang, Z. Yao, P. Chen, C. Zhou, Z. Li, *J. Alloys Compd.* **889**, 161734 (2022). <https://doi.org/10.1016/j.jallcom.2021.161734>
64. S. Bandaru, N. Murthy, R. Kulkarni, N.J. English, *J. Mater. Sci. Technol.* **86**, 127 (2021). <https://doi.org/10.1016/j.jmst.2021.01.041>

Springer Nature or its licensor (e.g. a society or other partner) holds exclusive rights to this article under a publishing agreement with the author(s) or other rightsholder(s); author self-archiving of the accepted manuscript version of this article is solely governed by the terms of such publishing agreement and applicable law.